Resonance Characterization and Frequency-divided Compensation Strategy for Heterogeneous Inverters-paralleled System

Hongbin Lin, Pingjuan Ge, Hailiang Xu, *Member*, *IEEE*, and Yuhan Duan

***Abstract*—Currently, the dominant trend in new energy power supply systems is the heterogeneous inverters-paralleled system (HIPS), which is a combination of grid-following (GFL) and grid-forming (GFM) inverters. The dynamic characteristics of different inverters in HIPS and the differences between GFL and GFM inverters undoubtedly increase the difficulty of the stability analysis and coordinated control. This paper establishes an interactive admittance matrix model of HIPS, fully considers the interactive effects among different inverters, and explores the multi-dimensional resonance characteristics of HIPS by utilizing the modal analysis method. To achieve the coordinated control and oscillation suppression among different inverters, a frequency-divided compensation strategy is proposed, which divides the operation modes of HIPS into three categories, i. e., GFM, GFL, and hybrid modes. Specifically, the frequency division boundary is determined based on the resonance characteristics of GFL and GFM inverters, with the operation modes of HIPS being dynamically adjusted according to the harmonic power ratio. Finally, the simulation and experimental results demonstrate that the HIPS can flexibly adjust the operation modes to adapt to the complex conditions after adopting the frequency-divided compensation strategy and suppressing the oscillation frequency ratio to less than 2%, ensuring the safe and reliable operation of HIPS.**

***Index Terms*—Grid-following (GFL) inverter, grid-forming (GFM) inverter, heterogeneous inverters-paralleled system (HIPS), frequency-divided compensation strategy.**

NOMENCLATURE

ω_1	Grid angular frequency
φ_{i0}	Phase of fundamental current
$\boldsymbol{\Lambda}$, λ_i	Diagonal eigenvalue matrix and eigenvalue
θ_{v1}	Phase of initial voltage
θ_{PSL}	Phase angle of power synchronization loop (PSL) in grid-forming (GFM) inverter
θ_{PLL}	Phase angle of phase-locked loop (PLL) in grid-following (GFL) inverter
$B_{\mathrm{PLL\text{-}GFL}}$	PLL bandwidth of GFL inverter
$B_{\mathrm{CL\text{-}GFL}}$	Current loop bandwidth of GFL inverter
$B_{\mathrm{VL\text{-}GFM}}$	Voltage loop bandwidth of GFM inverter
$B_{\mathrm{CL\text{-}GFM}}$	Current loop bandwidth of GFM inverter
$C_{\mathrm{p}}(s)$, $C_{\mathrm{n}}(s)$	Transfer functions of θ_{PSL} for positive- and negative-sequence voltage perturbations
C_v, R_{vc}	Virtual capacitance and resistance of $Z_{\mathrm{C}}(s)$
$C_{v\max}$	The maximum virtual capacitance of $Z_{\mathrm{C}}(s)$
d, q	Indices of d and q axes
E_r	Output voltage of PSL
f_{spwm}	Switching frequency
f_s	Grid frequency
$G_d(s)$	Equivalent transfer function of control delay links
$H_i(s)$	Transfer function of current loop in GFL inverter
$H_{\mathrm{PLL}}(s)$	Transfer function of PLL
$H_{vv}(s)$	Transfer function of voltage loop in GFM inverter
$H_{vc}(s)$	Transfer function of current loop in GFM inverter
I_0, V_0	Peak values of fundamental current and grid voltage
I_i	Equivalent output current of inverter i
$\boldsymbol{I}_f$	Node current matrix at frequency f
i_g, u_g	Grid-connected current and voltage
i_{g1}, i_{g2}	Grid-connected currents of GFL and GFM inverters
i_{dq1}, i_{dq2}	Grid-connected currents of GFL and GFM inverters in dq-axis
i_{gh}^h, i_{gl}^h	High- and low-frequency components of harmonic current
i_{dq1}^{ref}	Reference value of i_{dq1}
i_L	Converter output current
K_{P}	Equivalent coefficient of modulation link
$K_{p\mathrm{PLL}}$, $K_{i\mathrm{PLL}}$	Proportional and integral parameters of PLL

Manuscript received: April 19, 2024; revised: August 5, 2024; accepted: November 14, 2024. Date of CrossCheck: November 14, 2024. Date of online publication: November 28, 2024.

This work was supported by the National Natural Science Foundation of China (No. 52077222) and the Shandong Provincial Natural Science Foundation (No. ZR2023QE156).

H. Lin, P. Ge (corresponding author), H. Xu, and Y. Duan are with the College of New Energy, China University of Petroleum (East China), Qingdao 266580, China, and H. Lin is also with the Key Laboratory of Control of Power Transmission and Conversion, Ministry of Education, Shanghai Jiao Tong University, Shanghai 200240, China (e-mail: Linhongbin@s. upc. edu. cn; gepingjuan@upc.edu.cn; xuhl@upc.edu.cn; z23150039@s.upc.edu.cn).

DOI: 10.35833/MPCE.2024.000416

K_{pi}, K_{ii}	Proportional and integral parameters of current loop in GFL inverter
K_p, K_q	Active and reactive droop coefficients
K_{vpi}, K_{vii}	Proportional and integral parameters of voltage loop in GFM inverter
K_{cpi}, K_{cii}	Proportional and integral parameters of current loop in GFM inverter
k_c	Compensation coefficient of GFL inverter
k_v	Compensation coefficient of GFM inverter
$\boldsymbol{L}$, $\boldsymbol{T}$	Left and right eigenvector matrices, $\boldsymbol{L}=\boldsymbol{T}^{-1}$
L_{11}, C_{f1}, L_{12}	Parameters of LCL filter for GFL inverter
L_{21}, C_{f2}, L_{22}	Parameters of LCL filter for GFM inverter
L_v, R_{vl}	Virtual inductance and resistance of $Z_L(s)$
$L_{v\max}$	The maximum virtual inductance of $Z_L(s)$
n	Number of inverters
P_{ref}, P_e	Rated and actual active power
Q_{ref}, Q_e	Rated and actual reactive power
R_g, L_g	Grid resistance and inductance
S_F, S_H, S_L	Total system, high-frequency, and low-frequency harmonic power
S_{GFL}, S_{GFM}	Rated capacities of GFL and GFM converters
$T_p(s)$, $T_n(s)$	Transfer functions of θ_{PLL} for positive- and negative-sequence voltage perturbations
T_s	Sampling period
U_{ref}, ω_{ref}	Root mean square (RMS) values of line voltage and angular frequency
$\boldsymbol{U}_f$	Node voltage matrix at frequency f
$\boldsymbol{U}_s$	Node voltage matrix of heterogeneous inverters-paralleled system (HIPS)
u_{PCC}	Voltage of point of common coupling (PCC)
u_{dq}	Voltage of PCC in dq-axis
U_i	Equivalent output voltage of inverter i
U_{PCC}	Magnitude of U_{PCC}
x	Variable parameter for HIPS
$\boldsymbol{Y}$	Interactive admittance matrix of HIPS
$\boldsymbol{Y}_f$	Node admittance matrix at frequency f
Y_{ii}	Equivalent self-admittance of inverter i
$Y_{ij}\,(i\neq j)$	Admittance denoting interactive effect between inverters i and j
Y_{ig}	Admittance denoting interactive effect between inverter i and grid
$Y_{GFLp}(s)$, $Y_{GFLn}(s)$	Positive- and negative-sequence output admittances of GFL inverter
$Y_{GFMp}(s)$, $Y_{GFMn}(s)$	Positive- and negative-sequence output admittances of GFM inverter
Y_{si}	Equivalent output admittance of inverter i, representing $Y_{GFMp}(s)$ or $Y_{GFLp}(s)$
Z_g, Y_g	Grid equivalent impedance and admittance
$Z_L(s)$	Function of virtual resistance-inductance strategy
$Z_C(s)$	Function of virtual resistance-capacitance strategy

I. Introduction

THE grid-following (GFL) inverters serve as essential interfaces for integrating renewable energy sources into the power grid, thereby enhancing the utilization of renewable resources. However, the GFL inverters face notable limitations in supporting grid voltage and frequency [1], [2]. Consequently, the grid-forming (GFM) inverters have gained significant interest as a promising solution to regulating grid-connected inverters, particularly in systems with high renewable energy penetration [3], [4]. In such systems, the GFL and GFM inverters coexist for extended periods, forming a heterogeneous inverters-paralleled system (HIPS) [5].

HIPS combines the advantages of both GFL and GFM inverters, providing voltage and frequency supports along with rapid power responses. However, it also inherits the drawbacks associated with each type of inverter. For instance, GFL inverters are susceptible to high-frequency oscillations in weak grids [6], [7], while GFM inverters are prone to low-frequency oscillations in strong grids [8], [9]. Furthermore, the interactions among different types of inverters in the HIPS may lead to multi-dimensional oscillation issues that encompass both high and low frequencies. Therefore, in a heterogeneous system such as HIPS, which comprises various grid-connected inverters, the coordinated control among the inverters becomes crucial for optimizing the overall system performance.

Currently, numerous studies have been conducted on the small-signal stability of inverters-paralleled system. However, most of them focus on the equivalent model [10], instability mechanism [11], and analytical tools for single-type inverters-paralleled system [12]. In particular, the studies on GFL inverters-paralleled system mainly primarily emphasizes the phase-locked loop (PLL) control [13], and the studies on GFM inverters-paralleled system are mostly concentrated on the power synchronization loop (PSL) control, including droop control [14], virtual synchronization control [15], etc.

In addition to the aforementioned studies focusing on the characteristics of single-type inverters-paralleled systems, some researchers have conducted comparative analyses of these two types of inverters. In [16], the second-order simplified models for both GFL and GFM inverters have been established to analyze their grid-connected synchronous characteristics. However, the research on HIPS remains relatively scarce. Although an initial state-space matrix model of HIPS is developed to investigate the power penetration law in islanded systems [17], the state-space matrix modeling method involves too numerous state variables to be generalized to multi-type inverters-paralleled systems.

Apart from the time-domain state-space matrix modeling of HIPS in [17], the impedance modeling based on the frequency-domain impedance is more commonly applied in multi-type inverters-paralleled system. For instance, in [18], Norton equivalent circuit and nodal admittance matrix for GFL inverters-paralleled system are established, and the modal analysis is employed to qualitatively examine the influence of system parameters and control variables on stability. However, this approach only provides simplified modeling for GFL inverters-paralleled system, neglecting factors

such as PLL.

The coordinated control among different inverters can be categorized into power allocation and power quality management [19], [20]. The power allocation problem is particularly relevant in islanded systems, where a leader-follower consensus control is proposed in [6] to distribute power evenly between GFL and GFM inverters, with GFM inverter acting as the leader and GFL inverter as the follower. Although this control leverages the primary frequency modulation capabilities of GFL inverter, it reduces the energy utilization efficiency.

The power quality management involves the mitigation of harmonic issues, including high-frequency oscillations of GFL inverters-paralleled system in weak grids and low-frequency oscillations of GFM inverters-paralleled system in strong grids. To tackle these challenges, [21] categorizes the resonance types of GFL inverters-paralleled system into dynamic and static resonances and proposes a hybrid multi-resonance suppression strategy. However, this method is complicated in its calculations, requiring momentary adjustments to the suppression strategy. In [22], a voltage feed-forward phase compensation method is proposed for GFL inverters-paralleled system. However, it necessitates a trade-off between the harmonic attenuation and resonance destabilization. A conduction compensator is designed in [23] to enhance the damping performance of GFM inverters-paralleled system, thereby improving the dynamic performance under variations in power reference tracking and load disturbances. Nevertheless, the above studies addressing power quality are limited to single-type inverters and do not recognize that the actual power supply system is HIPS. Therefore, the coordinated control between these two types of inverters is crucial for optimizing the HIPS performance.

In summary, the existing research is limited to single-type inverters-paralleled system. The study on the HIPS stabilization mechanism needs to be sufficiently intensive, and the interactive mechanisms of different types of inverters need to be identified. Moreover, the corresponding coordinated control among different inverters requires improvement. In this regard, the specific contributions of this paper are as follows.

1) This paper establishes an interactive admittance matrix model of HIPS. This model introduces the self-admittance to represent the equivalent effect of the inverters themselves and mutual admittance to characterize the interactions among different inverters, thereby capturing the dynamic interactive characteristics of HIPS more accurately.

2) This paper investigates the multi-dimensional resonance characteristics of HIPS through modal analysis and parameter sensitivity analysis methods. It analyzes the dominant factors contributing to oscillatory destabilization under different operating conditions and examines the interactive mechanisms of GFL and GFM inverters.

3) This paper proposes a frequency-divided compensation strategy for HIPS. This strategy flexibly adjusts the operation mode according to the ratio of high-frequency harmonic power to low-frequency harmonic power, reduces the oscillation frequency ratio to less than 2%, and ensures the safe, reliable, and stable operation of HIPS.

This paper is organized as follows. The interactive admittance matrix model of HIPS is established in Section II. Section III explores the HIPS stability and identifies the dominant factors using modal analysis and parameter sensitivity analysis, and Section IV proposes a frequency-divided compensation strategy for the HIPS. Simulation and experimental results are given in Section V. Finally, Section VI draws conclusions.

II. Interactive Admittance Matrix Model of HIPS

The structure of HIPS is illustrated in Fig. 1, including the GFL inverter, GFM inverter, and the power grid. It can be observed that the GFL inverter employs a PLL to achieve synchronization, and the GFM inverter utilizes the PSL to achieve self-synchronization [24]. It is noteworthy that both GFL and GFM inverters are controlled based on *dq*-axis. SPWM is short for sinusoidal pulse-width modulation.

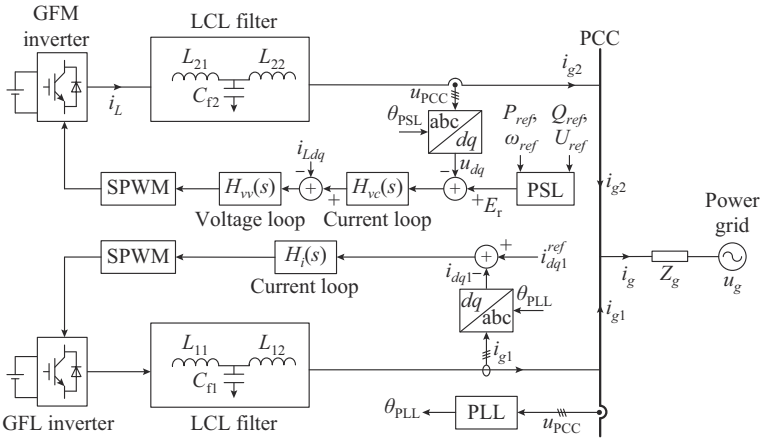

Fig. 1. Structure of HIPS.

A. Sequential Admittance Model of GFL Inverter

As illustrated in Fig. 1, the GFL inverter adopts the typical PLL based on the synchronized coordinate system and the current-loop control based on the *dq* coordinate system. The transfer function of PLL, i. e., $H_{PLL}(s)$, can be expressed as (1), whose structure depicted in Appendix A Fig. A1 [25].

$$H_{PLL}(s)=\frac{K_{pPLL}+K_{iPLL}/s}{s} \tag{1}$$

The harmonic linearization method is capable of modeling the PLL and the current loop while also accounting for the influence of control delay. This paper draws upon the comprehensive derivation of the PLL-based sequence-impedance model for GFL inverters outlined in [26], hence the detailed derivation process is not reiterated here. The positive- and negative-sequence output admittances of GFL inverters, i.e., $Y_{\mathrm{GFLp}}(s)$ and $Y_{\mathrm{GFLn}}(s)$, respectively, are obtained and presented as:

$$\begin{cases} Y_{\mathrm{GFLp}}(s)=\dfrac{Y_1(s)-K_{\mathrm{P}}\left(H_i(s-\mathrm{j}\omega_1)G_d(s)+\dfrac{V_0}{I_0\mathrm{e}^{\mathrm{j}\varphi_{i0}}}\right)T_{\mathrm{p}}(s)I_0\mathrm{e}^{\mathrm{j}\varphi_{i0}}}{Y_2(s)+K_{\mathrm{P}}H_i(s-\mathrm{j}\omega_1)G_d(s)} \\ Y_{\mathrm{GFLn}}(s)=\dfrac{Y_1(s)-K_{\mathrm{P}}\left(H_i(s+\mathrm{j}\omega_1)G_d(s)+\dfrac{V_0}{I_0\mathrm{e}^{-\mathrm{j}\varphi_{i0}}}\right)T_{\mathrm{n}}(s)I_0\mathrm{e}^{-\mathrm{j}\varphi_{i0}}}{Y_2(s)+K_{\mathrm{P}}H_i(s+\mathrm{j}\omega_1)G_d(s)} \end{cases} \tag{2}$$

where $T_{\mathrm{p}}(s)$ and $T_{\mathrm{n}}(s)$ are detailed in Appendix B (B1); $Y_1(s)$ and $Y_2(s)$ are detailed in Appendix B (B2); and $G_d(s)$ is expressed as:

$$G_d(s)=\frac{1-\mathrm{e}^{-sT_s}}{sT_s}\mathrm{e}^{-sT_s}\approx\mathrm{e}^{-1.5sT_s} \tag{3}$$

The current loop adopts a proportional-integral (PI) controller, which is expressed as:

$$H_i(s)=K_{pi}+\frac{K_{ii}}{s} \tag{4}$$

B. Sequential Admittance Model of GFM Inverter

As illustrated in Fig. 1, the PSL of GFM inverter employs typical droop control for self-synchronization, with its detailed structure depicted in Appendix A Fig. A2. The transfer function representing the principle of droop control is expressed as [27]:

$$\begin{cases} \theta_{\mathrm{PSL}}(s)=\dfrac{\omega_{ref}-K_p(P_e-P_{ref})}{s} \\ E_r(s)=U_{ref}-K_q(Q_e-Q_{ref}) \end{cases} \tag{5}$$

Since the inverters are connected to the PCC in parallel, the calculation of admittance in this circuit is simplified. Furthermore, the output characteristics of a GFM inverter can be expressed in terms of admittance. The positive- and negative-sequence output admittances of GFM inverters, i.e., $Y_{\mathrm{GFMp}}(s)$ and $Y_{\mathrm{GFMn}}(s)$, respectively, are derived based on [27] as:

$$\begin{cases} Y_{\mathrm{GFMp}}(s)= \\ \quad\dfrac{Y_3(s)+K_{\mathrm{P}}(H_{vc}(s-\mathrm{j}\omega_1)H_{vv}(s-\mathrm{j}\omega_1)-C_{\mathrm{p}}(s)I_0\mathrm{e}^{-\mathrm{j}\varphi_{i0}})G_d(s)}{Y_4(s)+K_{\mathrm{P}}(H_{vc}(s-\mathrm{j}\omega_1)+C_{\mathrm{p}}(s)V_0)G_d(s)} \\ Y_{\mathrm{GFMn}}(s)= \\ \quad\dfrac{Y_3(s)+K_{\mathrm{P}}(H_{vc}(s+\mathrm{j}\omega_1)H_{vv}(s+\mathrm{j}\omega_1)+C_{\mathrm{n}}(s)I_0\mathrm{e}^{-\mathrm{j}\varphi_{i0}})G_d(s)}{Y_4(s)+K_{\mathrm{P}}(H_{vc}(s+\mathrm{j}\omega_1)+C_{\mathrm{n}}(s)V_0)G_d(s)} \end{cases} \tag{6}$$

where $C_{\mathrm{p}}(s)$, $C_{\mathrm{n}}(s)$, $Y_3(s)$, and $Y_4(s)$ are elaborated in Appendix B (B3)-(B7). The voltage loop $H_{vv}(s)$ and current loop $H_{vc}(s)$ are defined as:

$$\begin{cases} H_{vv}(s)=K_{vpi}+\dfrac{K_{vii}}{s} \\ H_{vc}(s)=K_{cpi}+\dfrac{K_{cii}}{s} \end{cases} \tag{7}$$

C. Interactive Admittance Matrix Model of HIPS

To further investigate the interactive mechanism between GFL and GFM inverters, this paper establishes the interactive admittance matrix model of HIPS. As depicted in Fig. 2, this model introduces the mutual admittance $Y_{ij}(i\neq j)$ to represent the interactive effect between inverters and introduces the mutual admittance Y_{ig} to represent the interactive effect between inverters and the power grid. The interactive admittance matrix of HIPS can be derived as (8).

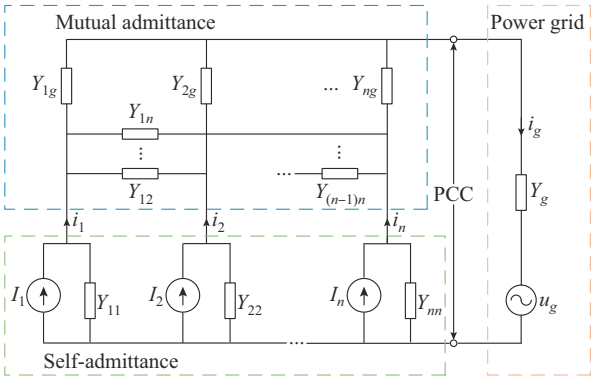

Fig. 2. Norton equivalent circuit for HIPS considering interactive effects.

$$\begin{bmatrix} I_1 \\ I_2 \\ \vdots \\ I_n \\ U_{\mathrm{PCC}}Y_g \end{bmatrix}=\begin{bmatrix} Y_{11} & Y_{12} & \cdots & Y_{1n} & Y_{1g} \\ Y_{21} & Y_{22} & \cdots & Y_{2n} & Y_{2g} \\ \vdots & \vdots & & \vdots & \vdots \\ Y_{n1} & Y_{n2} & \cdots & Y_{nn} & Y_{ng} \\ Y_{g1} & Y_{g2} & \cdots & Y_{gn} & Y_g \end{bmatrix}\begin{bmatrix} U_1 \\ U_2 \\ \vdots \\ U_n \\ U_{\mathrm{PCC}} \end{bmatrix}=\boldsymbol{Y}\boldsymbol{U}_s \tag{8}$$

where $Y_{gi}=Y_{ig}$.

Note that because the line inductor is in series with the grid-side filter inductor, it can be directly added to the grid-side filter inductor [28], which further facilitates the analysis of the HIPS stabilization mechanism. To facilitate theoretical calculations and expressions, the grid impedance is described in the admittance form Y_g. The nonzero elements are expressed as:

$$\begin{cases} Y_{ii}=Y_{si}//\displaystyle\sum_{j=1,j\neq i}^{n}Y_{sj} \\ Y_{ij,i\neq j}=-\left(Y_{si}//\displaystyle\sum_{j=1,j\neq i}^{n}Y_{sj}\right)\left(Y_{sj}\Big/\displaystyle\sum_{j=1,j\neq i}^{n}Y_{sj}\right) \\ Y_{ig}=-\left(Y_{si}//\displaystyle\sum_{j=1,j\neq i}^{n}Y_{sj}\right)\left(Y_{g}\Big/\displaystyle\sum_{j=1,j\neq i}^{n}Y_{sj}\right) \end{cases} \tag{9}$$

where the symbol "//" indicates a parallel connection. Notably, the positive-sequence admittance of the inverter provides more comprehensive information regarding its output characteristics [29]. Therefore, to simplify the arithmetic process, the positive-sequence admittance of the inverter will serve as an example for analyzing the resonance characteris-

tics of HIPS.

III. Stability Analysis and Identification of Dominant Factors

This section employs the modal analysis and parameter sensitivity analysis to investigate the oscillation characteristics of HIPS and identify the dominant factors. Specifically, the HIPS comprises one GFL inverter and one GFM inverter, with their parameters detailed in Table I.

TABLE I
Parameters of HIPS

Parameter type	Symbol	Value
GFL inverter	S_{GFL}	10 kW
	K_{pPLL}, K_{iPLL}	1, 80
	K_{pi}, K_{ii}	2, 120
GFM inverter	S_{GFM}	10 kW
	K_p, K_q	5×10^{-3}, 2×10^{-3}
	K_{vpi}, K_{vii}	1, 20
	K_{cpi}, K_{cii}	5, 100
LCL filter	L_{11}, L_{21}	3.5 mH
	C_{f1}, C_{f2}	30 μF
	L_{12}, L_{22}	0.33 mH
Runtime environment	U_{PCC}, f_s	380 V, 50 Hz
	R_g, L_g	0.2 Ω, 0.5-20 mH
	T_s	1×10^{-5} s
	f_{spwm}	10 kHz

A. Modal Analysis and Parameter Sensitivity Analysis

The modal analysis method can be described as follows [18]. In a multi-node system, the harmonic resonance typically occurs when the network node admittance matrix $\boldsymbol{Y}$ contains very small values. In extreme cases, the matrix $\boldsymbol{Y}$ approaches singularity, resulting in significantly large values in $\boldsymbol{Y}^{-1}$. Assuming the resonance occurs at a frequency f, the nodal voltage-current equation of HIPS can be expressed as:

$$\boldsymbol{U}_f = \boldsymbol{Y}_f^{-1}\boldsymbol{I}_f \tag{10}$$

$\boldsymbol{Y}_f$ can be decomposed into the following form:

$$\boldsymbol{Y}_f = \boldsymbol{L}\boldsymbol{\Lambda}\boldsymbol{T} \tag{11}$$

where $\boldsymbol{\Lambda} = \mathrm{diag}(\lambda_1, \lambda_2, ..., \lambda_n)$. Notably, the eigenvalues derived from the inverse of the node admittance matrix have impedance characteristics, which are defined as modal impedance (MI). MI denotes the ratio of voltage to current for a particular oscillatory mode of HIPS, and a large MI value indicates that the HIPS responds more dramatically to current variations in that mode, which may lead to system destabilization.

The modal analysis method involves solving the eigenvalues of the node admittance matrix $\boldsymbol{Y}$ across the entire frequency spectrum and subsequently plotting the distribution of these eigenvalues. This visualization aids in the analysis of the oscillation characteristics of HIPS.

Furthermore, to identify the dominant factors of HIPS, the parameter sensitivity analysis is essential. A commonly employed approach for conducting such analysis involves computing the eigenvalue matrix of the partial derivatives of the relevant parameters [30]. This paper adopts the conventional normalization method for parameter sensitivities, enabling their expression in percentages to better elucidate the degree of their respective influences. The normalized sensitivities can be described as:

$$\frac{\partial|\lambda|}{\partial x} = \frac{\partial|\lambda_i|/|\lambda_i|}{\partial x/x} = \frac{\partial|\lambda_i|}{\partial x}\frac{x}{|\lambda_i|} \tag{12}$$

Figure 3 depicts the flowchart of the modal analysis and parameter sensitivity analysis. Specifically, during the modal analysis, this paper defines the frequency range $[f_1, f_2]$= [1, 104]Hz and the frequency step $\Delta f = 5$ Hz to analyze the accuracy requirements [31]. During the parameter sensitivity analysis, this paper gives the short-circuit ratio (SCR) range as $[M_1, M_2]$=[2, 6] with a step of $\Delta M = 0.5$.

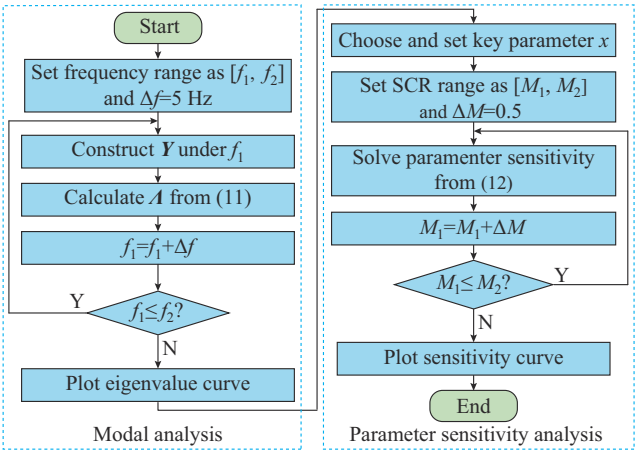

Fig. 3. Flowchart of modal analysis and parameter sensitivity analysis.

It is noteworthy that the quantitative analysis of the sensitivity of critical parameters can yield positive or negative results, which can be interpreted as follows. A positive sensitivity indicates a positive correlation, suggesting that an increase in the parameter leads to a rise in its equivalent negative impedance, thus increasing the risk of system destabilization. Conversely, a negative sensitivity indicates the opposite trend.

B. Stability Estimation of HIPS

The HIPS, consisting of GFL and GFM inverters, integrates the advantages of these two inverters and also retains the inherent instability risks associated with each inverter under varying SCR conditions. Consequently, this paper employs the modal analysis to investigate the oscillation characteristics and conducts parameter sensitivity analysis based on the interactive admittance matrix model of HIPS.

Figure 4 illustrates the stability analysis results of HIPS under various SCRs, revealing three resonance peaks identified as States I, II, and III, respectively. When combined with the parameter sensitivity analysis results in Fig. 5, several observations emerge.

1) State I: as SCR increases, the risk of GFM inverter destabilization in the low-frequency band intensifies. The parameter sensitivity analysis indicates that the primary cause of destabilization in the low-frequency band is the destabilization of the voltage loop due to the minimum grid imped-

ance. Notably, according to (13), a decrease in inductive reactance value X_{L} leads to a rise in the instantaneous reactive power Q_{L} with a constant voltage U_{PCC}. Consequently, the PSL experiences significant power fluctuations, triggering detuning destabilization, which further results in voltage loop destabilization.

$$Q_{\mathrm{L}} = U_{\mathrm{PCC}}^2 / X_{\mathrm{L}} \tag{13}$$

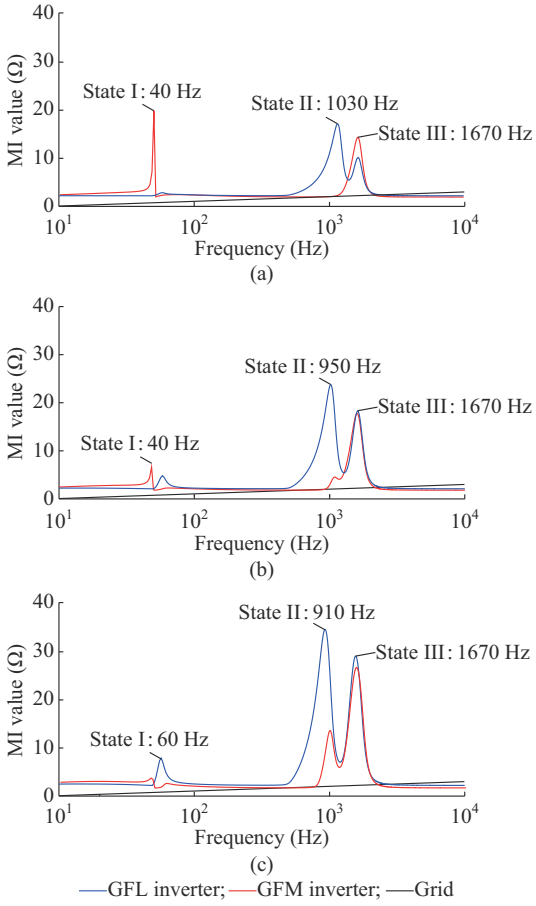

Fig. 4. Modal analysis of HIPS under different SCRs. (a) $SCR = 6$. (b) $SCR = 4$. (c) $SCR = 2$.

2) State II: an increase in grid impedance will exacerbate the coupling effect between the HIPS and the grid impedance, leading to resonance instability rapidly occurring in the mid- and high-frequency bands. The parameter sensitivity analysis reveals that the dominant factor determining the occurrence of resonance instability in this scenario is the bandwidth of the current loops of both types of inverters. However, the dominant factor contributing to resonance instability in this instance is the current loop of GFL inverter, attributing to the clamping effect of the voltage loop of GFM inverter.

3) State III: this resonant instability point is caused by the resonance of LCL filter in the inverter, whose resonance frequency f_{LCL} is calculated as (14). The coupling between the LCL filter and grid impedance intensifies as grid impedance increases.

$$f_{\mathrm{LCL}} = \frac{1}{2\pi}\sqrt{(L_{11}+L_{12})/(L_{11}L_{12}C_{\mathrm{fl}})} \tag{14}$$

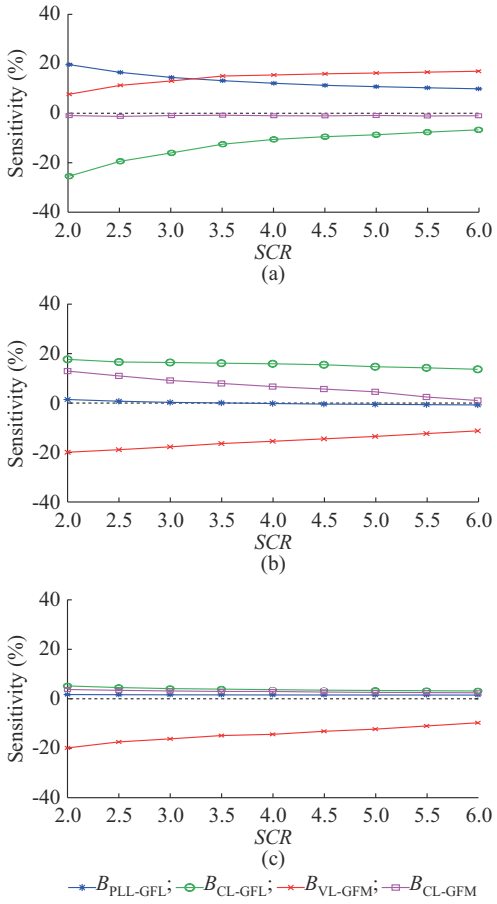

Fig. 5. Parameter sensitivity analysis of HIPS under different states. (a) State I. (b) State II. (c) State III.

In summary, the HIPS is susceptible to high-frequency resonance instability under weak grid conditions, which is essentially caused by the increased coupling between the current loop of GFL inverter and the grid impedance. Conversely, the HIPS is prone to low-frequency resonance instability under strong grid conditions, primarily stemming from the small grid impedance that destabilizes the voltage loop of GFM inverter.

IV. Frequency-Divided Compensation Strategy

Considering the multi-dimensional resonance characteristics of HIPS, it is evident that GFL inverter primarily drives high-frequency resonance, while GFM inverter is responsible for low-frequency oscillations, categorized as sub-synchronous oscillations [32]. The boundary for frequency division is designated as 200 Hz, which is not strictly defined and resulted from weighing the output characteristics of HIPS.

As depicted in Fig. 6, firstly, the harmonic components i_g^h are extracted with the second-order generalized integrator (SOGI) and divided by a low-pass filter (LPF), obtaining i_{gh}^h and i_{gl}^h. Secondly, the high-frequency harmonic power (S_{H}) and low-frequency harmonic power (S_{L}) are calculated through power analysis. Finally, the compensation coefficients of these two inverters are assigned by the compensation coefficient command in (15).

$$\begin{cases} k_v=0, k_c=1 & |S_{\mathrm{H}}|\geq 4\%|S_{\mathrm{F}}|, |S_{\mathrm{L}}|\leq 1\%|S_{\mathrm{F}}| \\ k_c, k_v\in(0,1) & |S_{\mathrm{H}}|\geq 1\%|S_{\mathrm{F}}|, |S_{\mathrm{L}}|\geq 1\%|S_{\mathrm{F}}|, |S_{\mathrm{H}}|+|S_{\mathrm{L}}|\geq 5\%|S_{\mathrm{F}}| \\ k_c=0, k_v=1 & |S_{\mathrm{L}}|\geq 4\%|S_{\mathrm{F}}|, |S_{\mathrm{H}}|\leq 1\%|S_{\mathrm{F}}| \end{cases} \tag{15}$$

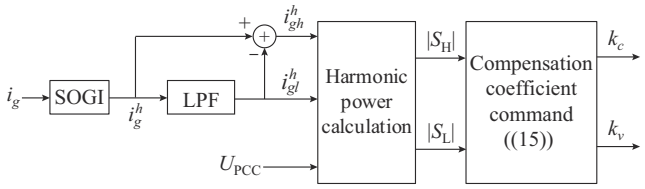

Fig. 6. Frequency-divided complementary control block diagram of HIPS.

Notably, according to the inverter grid-connected guidelines, the harmonic content of the grid-connected current must not exceed 5%. Therefore, when designing the operation mode boundary, the upper limit of harmonic content cannot exceed 5% of the total power, i. e., $|S_{\mathrm{L}}|+|S_{\mathrm{H}}|\leq 5\%|S_{\mathrm{F}}|$. Additionally, to achieve the reasonable control and harmonic suppression effect, the lower limit of single-type harmonics is bounded to less 1% of the total power, i. e., $|S_{\mathrm{L}}|\leq 1\%|S_{\mathrm{F}}|$ and $|S_{\mathrm{H}}|\leq 1\%|S_{\mathrm{F}}|$, as illustrated in Fig. 7. Corresponding to (15), Fig. 7 categorizes the operation modes into four types: GFM, hybrid, GFL, and stabilized modes. The stabilized mode remains unchanged, as it does not require oscillation suppression.

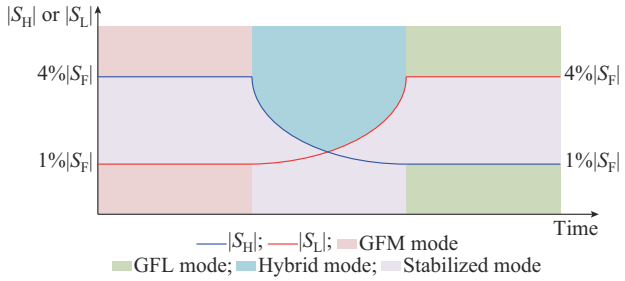

Fig. 7. Different operation modes of HIPS.

Figure 8 illustrates the specific implementation of the frequency-divided complementary strategy. The implementation steps of the specific mode are as follows.

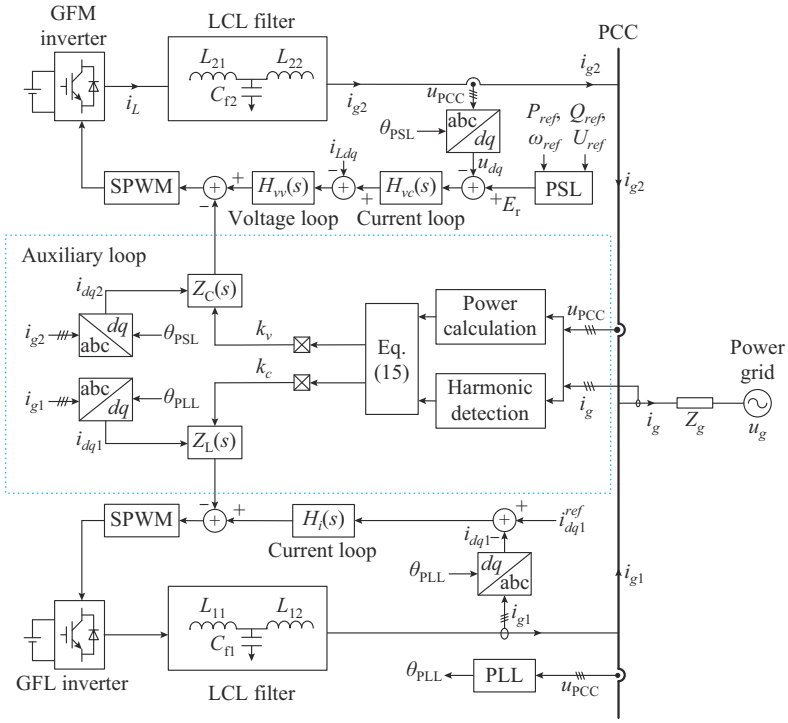

Fig. 8. Specific implementation of frequency-divided compensation strategy.

1) To address the high-frequency resonance instability in weak grids, an auxiliary loop is incorporated into the dominant GFL inverter. This approach involves introducing the virtual resistance-inductance strategy to address high-frequency resonance without altering the GFM inverter. This mode is referred to as the GFM mode, encompassing both the GFM inverter and the compensated GFL inverter.

2) To address the low-frequency oscillation instability in strong grids, an auxiliary loop is introduced for the dominant GFM inverter. This approach involves introducing the virtual resistance-capacitance strategy to suppress low-frequency resonance while maintaining the GFL inverter unchanged. This mode is referred to as the GFL mode, comprising both the GFL inverter and the compensated GFM inverter.

3) When both high- and low-frequency resonances are present, the HIPS is classified as a hybrid model. In this configuration, both inverters are compensated by implementing auxiliary loops to resolve grid quality issues. The compensation factors for both inverters can be evenly allocated according to the levels of high- and low-frequency harmonic power.

Figure 9 illustrates the flowchart of the frequency-divided

compensation strategy for HIPS, which utilizes harmonic power to dynamically adjust operation mode.

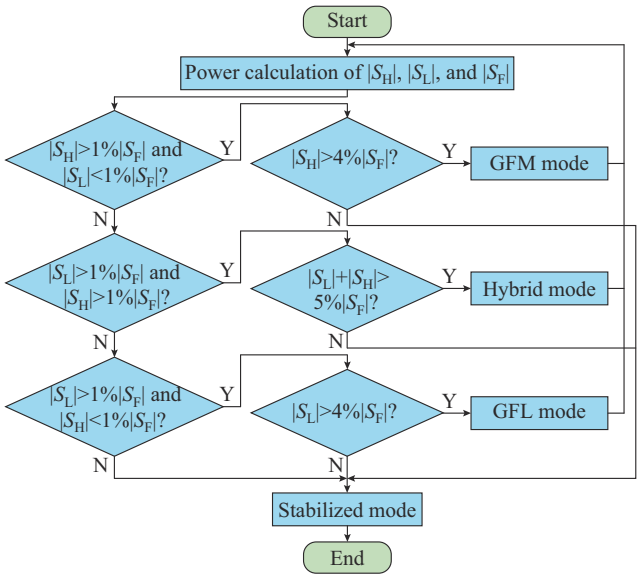

Fig. 9. Flowchart of frequency-divided compensation strategy for HIPS.

A. GFM Mode

In power systems, a lower equivalent input conductance improves the resistance to load variations, thereby enhancing the overall system stability. Given that the inductance has the property of passing low frequencies while blocking high frequencies, the increase of the inductance value in the power system can effectively reduce the equivalent input conductance, thereby improving anti-interference capabilities and stability.

Additionally, the research indicates that incorporating virtual inductance along with virtual resistance, to a certain extent, eliminates the negative damping effect of either virtual inductance or virtual resistance alone and improves the adjustment range of both values [33]. Thus, adding the virtual inductance to the control loop is undoubtedly the most economically viable choice.

Define the function of virtual resistance-inductance strategy as $Z_L(s)$:

$$Z_L(s)=R_{vl}+sL_v \tag{16}$$

As illustrated in Fig. 8, after incorporating $Z_L(s)$ to the GFL control loop, the equivalent positive- and negative-sequence admittances of GFL inverter can be expressed as:

$$\begin{cases} Y'_{GFLp}(s)= \\ \dfrac{Y_1(s)-K_P\left(H_i(s-j\omega_1)G_d(s)+\dfrac{V_0}{I_0e^{j\varphi_{i0}}}-Z_L(s)\right)T_p(s)I_0e^{j\varphi_{i0}}}{Y_2(s)+K_PH_i(s-j\omega_1)G_d(s)} \\ Y'_{GFLn}(s)= \\ \dfrac{Y_1(s)-K_P\left(H_i(s+j\omega_1)G_d(s)+\dfrac{V_0}{I_0e^{-j\varphi_{i0}}}-Z_L(s)\right)T_n(s)I_0e^{-j\varphi_{i0}}}{Y_2(s)+K_PH_i(s+j\omega_1)G_d(s)} \end{cases} \tag{17}$$

It is noticeable from Fig. 10 that as L_v increases, the resonance in the high-frequency range is effectively dampened; however, the risk of resonance in the low-frequency range escalates.

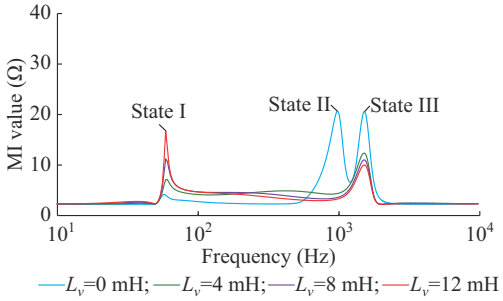

Fig. 10. Effect of different L_v values on stability of GFL inverter.

From the perspective of physical characteristics, since $Z_L(s)$ is implemented through the negative feedback link of grid current, the virtual inductance L_v is added to diminish the influence of grid inductance L_g. However, excessively large values of L_v may lead to system oscillations in the low-frequency range. Therefore, the value of L_v must be constrained. This paper illustrates the constraint curves of L_v with R_{vl} ($SCR=2$) and L_g ($R_{vl}=0\ \Omega$), as shown in Fig. 11.

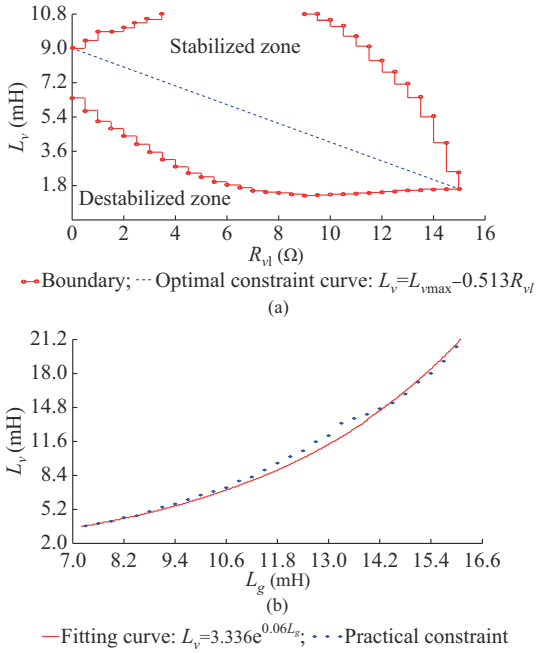

Fig. 11. Constraint curves of L_v with R_{vl} and L_g. (a) With R_{vl} ($SCR=2$). (b) With L_g ($R_{vl}=0\ \Omega$).

By analyzing Fig. 11(a) and (b), the constraint of L_v with R_{vl} and L_g can be expressed as (18). Notably, the flowchart for drawing the constraint is illustrated in Supplementary Material A Fig. S1.

$$L_v=L_{vmax}-0.513R_{vl}\approx 3.3e^{0.06L_g}-0.513R_{vl} \tag{18}$$

Furthermore, the value of R_{vl} can be determined based on the relationship between the high-frequency harmonic power and the grid-connected current, as shown in (19).

$$R_{vl}=\frac{|S_{\mathrm{H}}|}{1.5i_{gd}^2} \tag{19}$$

In summary, the value of $Z_{\mathrm{L}}(s)$ implemented in the GFM mode can be expressed as (20). This strategy dynamically adjusts the values of virtual inductance and resistance based on grid impedance and high-frequency harmonic power, demonstrating the robust dynamic performance and environmental adaptability.

$$Z_{\mathrm{L}}(s)=\frac{|S_{\mathrm{H}}|}{1.5i_{gd}^2}+s\left(3.3\mathrm{e}^{0.06L_g}-0.5\frac{|S_{\mathrm{H}}|}{1.5i_{gd}^2}\right) \tag{20}$$

B. GFL Mode

The GFL mode is designed to suppress low-frequency oscillations in the HIPS. Considering that capacitance has the characteristic of passing high frequencies while blocking low frequencies, along with its economic benefits, an auxiliary loop with virtual capacitances is constructed for the GFM inverter to suppress low-frequency oscillations. Similarly, the function of virtual resistance-capacitance strategy $Z_{\mathrm{C}}(s)$ can be expressed as:

$$Z_{\mathrm{C}}(s)=C_v^{-1}s^{-1}+R_{vc} \tag{21}$$

With the incorporation of $Z_{\mathrm{C}}(s)$ in the control loop of GFM inverter, the equivalent positive- and negative-sequence conductances of GFM inverter can be expressed as:

$$\begin{cases} Y'_{\mathrm{GFMp}}(s)=\dfrac{Y_3(s)}{Y_4(s)+K_{\mathrm{P}}(H_{vc}(s-\mathrm{j}\omega_1)+C_{\mathrm{p}}(s)V_0)G_d(s)}+ \\ \quad \dfrac{K_{\mathrm{P}}(H_{vc}(s-\mathrm{j}\omega_1)H_{vv}(s-\mathrm{j}\omega_1)-C_{\mathrm{p}}(s)I_0\mathrm{e}^{-\mathrm{j}\varphi_{i0}}-Z_{\mathrm{C}}(s))G_d(s)}{Y_4(s)+K_{\mathrm{P}}(H_{vc}(s-\mathrm{j}\omega_1)+C_{\mathrm{p}}(s)V_0)G_d(s)} \\ Y'_{\mathrm{GFMn}}(s)=\dfrac{Y_3(s)}{Y_4(s)+K_{\mathrm{P}}(H_{vc}(s+\mathrm{j}\omega_1)+C_{\mathrm{n}}(s)V_0)G_d(s)}+ \\ \quad \dfrac{K_{\mathrm{P}}(H_{vc}(s+\mathrm{j}\omega_1)H_{vv}(s+\mathrm{j}\omega_1)+C_{\mathrm{n}}(s)I_0\mathrm{e}^{-\mathrm{j}\varphi_{i0}}-Z_{\mathrm{C}}(s))G_d(s)}{Y_4(s)+K_{\mathrm{P}}(H_{vc}(s+\mathrm{j}\omega_1)+C_{\mathrm{n}}(s)V_0)G_d(s)} \end{cases} \tag{22}$$

From the analysis of physical characteristics, it is evident that $Z_{\mathrm{C}}(s)$ is obtained through the current feedback link. The addition of virtual capacitance C_v effectively reduces the capacitive negative damping of GFM inverter in the low-frequency range. However, excessively large values of capacitance can easily trigger high-frequency oscillations due to the inherent physical characteristics of capacitance, as illustrated in Fig. 12.

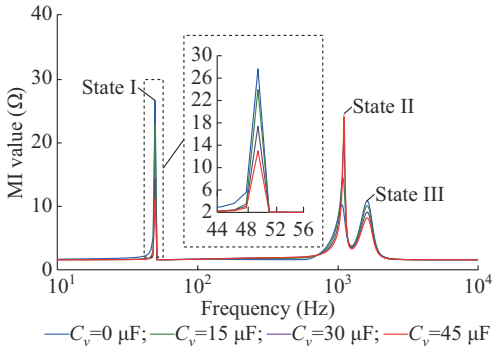

Fig. 12. Effect of different C_v values on stability of GFM inverter.

Consistent with the above analytical process, this paper examines the constraints of virtual capacitance C_v with R_{vc} and L_g, as shown in Fig. 13.

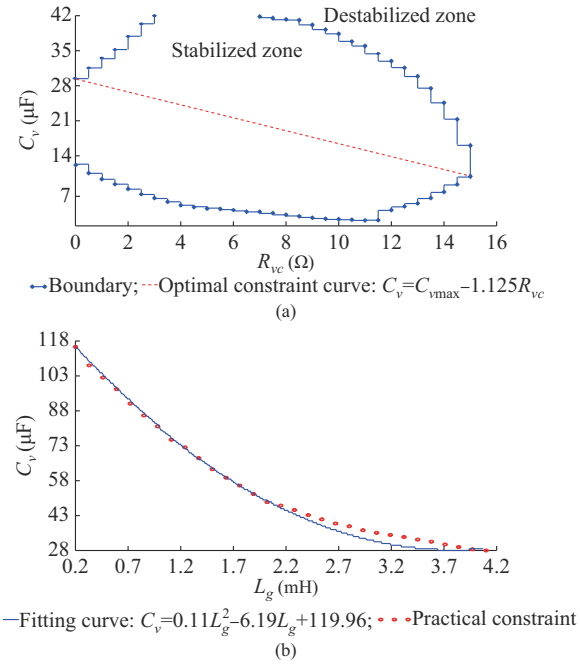

Fig. 13. Constraint curves of C_v with R_{vc} and L_g. (a) With R_{vc} ($SCR=6$). (b) With L_g ($R_{vc}=0$ Ω).

$$C_v=C_{v\max}-1.125R_{vc}\approx 0.11L_g^2-6.19L_g+119.96-1.125R_{vc} \tag{23}$$

The value of R_{vc} is determined as:

$$R_{vc}=\frac{|S_{\mathrm{L}}|}{1.5i_{gd}^2} \tag{24}$$

In summary, $Z_{\mathrm{C}}(s)$ in GFL mode can be expressed as:

$$Z_{\mathrm{C}}(s)=\frac{|S_{\mathrm{L}}|}{1.5i_{gd}^2}+\left(0.11L_g^2-6.19L_g+119.96-1.1\frac{|S_{\mathrm{L}}|}{1.5i_{gd}^2}\right)^{-1}s^{-1} \tag{25}$$

C. Hybrid Model

In the event of simultaneous high- and low-frequency oscillations in the HIPS, it is necessary to compensate both the GFL and GFM inverters. Specifically, the compensation coefficients of both inverters can be determined based on the high- and low-frequency harmonic contents. However, accurately measuring these harmonic contents in practical applications poses significant challenges. Therefore, this paper adjusts the compensation coefficients based on high- and low-frequency harmonic power, as illustrated in Fig. 14.

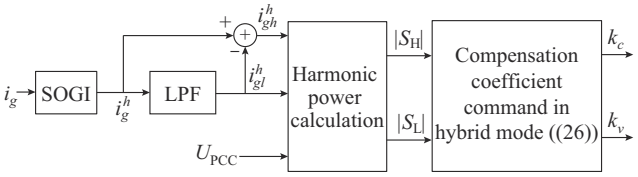

Fig. 14. Distribution of compensation coefficient in hybrid mode.

The compensation coefficients of HIPS for different inverters in hybrid mode are standardized, as shown in (26). When the HIPS exhibits a greater high-frequency harmonic content than low-frequency one, the corresponding compensation coefficient k_c for GFL inverter is higher than k_v for GFM inverter.

$$\begin{cases} |S_{\mathrm{H}}| \geq 1\% |S_{\mathrm{F}}| \\ |S_{\mathrm{L}}| \geq 1\% |S_{\mathrm{F}}| \\ |S_{\mathrm{H}}| + |S_{\mathrm{L}}| \geq 5\% |S_{\mathrm{F}}| \\ |S_{\mathrm{H}}| : |S_{\mathrm{L}}| = k_c : k_v \\ k_c + k_v = 1 \end{cases} \tag{26}$$

In summary, this approach adjusts the operation modes based on system frequency detection and harmonic power calculations. This approach ensures that the HIPS demonstrates the GFL characteristics under strong grid conditions and GFM characteristics under weak grid conditions.

V. Simulation and Experiment Verifications

This paper builds an HIPS simulation model and an experimental platform to verify the dominant factors contributing to resonant instability and the effectiveness of frequency-divided compensation strategy for HIPS. The HIPS is constructed based on MATLAB/Simulink, utilizing the physical parameters listed in Table I. Notably, the experimental validation results for the stability domain and sensitivity of key parameters are presented in Supplementary Material A Section B. Furthermore, this paper verifies the accuracy of the HIPS model through the nodal current injection method, as elaborated in Supplementary Material A Section C.

The experimental platform comprises two DC sources, two inverters, two LCL filters, an inductance, a transformer, and a host computer, as shown in Fig. 15. Two inverters are paralleled at the PCC and connected to the power grid via the transformer. Specifically, each converter includes a power module, a sampling module, a communication module, and a control module.

The high-frequency, low-frequency, and hybrid oscillations in HIPS are influenced by control parameters and operation conditions, which are not fixed. Therefore, the control parameters of HIPS and the operation conditions presented in Table II are used to assess the effectiveness of the frequency-divided compensation strategy.

Figure 16(a) illustrates the output currents i_a, i_b, and i_c of HIPS and the FFT analysis results both before and after the implementation of GFL mode in response to low-frequency instability under Case I. Notably, through the integration of the virtual resistance-capacitance into the GFM inverter, the oscillations of HIPS at 40 Hz are reduced from 7.7% to 1.2% after the transition to the GFL mode, demonstrating significant suppression of the oscillations. Similarly, it is observed from Fig. 16(b) that the oscillations at 910 Hz and 1670 Hz are significantly suppressed to less than 0.3% following the transition to the GFM mode. Figure 16(c) illustrates that the hybrid oscillation frequencies include 40 Hz, 950 Hz, and 1670 Hz, all of which are suppressed to less than 0.5% following the transition to the hybrid mode, further illustrating the effectiveness of the frequency-divided compensation strategy.

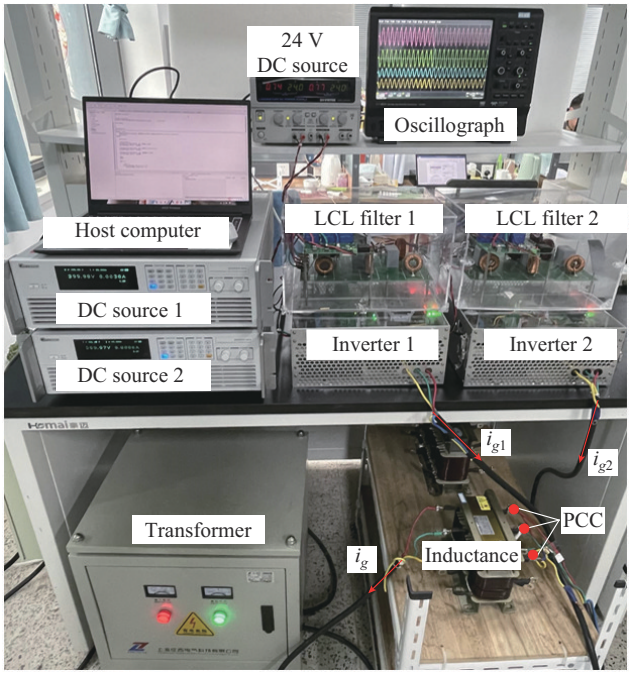

Fig. 15. Layout of experimental platform.

TABLE II
Control Parameters of HIPS and Operation Conditions

Case	GFL inverter		GFM inverter		SCR
	$B_{\text{PLL-GFL}}$ (Hz)	$B_{\text{CL-GFL}}$ (Hz)	$B_{\text{VL-GFM}}$ (Hz)	$B_{\text{CL-GFM}}$ (Hz)	
I	50	10	80	200	6
II	50	100	40	200	2
III	50	10	40	200	4

Figure 17(a) presents the comparison results of the output currents of HIPS and voltages at PCC accessing the GFL mode when low-frequency instability occurs under Case I. It can be noticed that the oscillation frequency content at 35 Hz is reduced from 5.8% to 0.7%. Additionally, Fig. 16(a) indicates that the HIPS oscillates at 40 Hz, while the experimental result shows at 35 Hz. Although this slight discrepancy exists, it does not affect the effectiveness of the strategy.

It is observed from Fig. 17(b) that the oscillation frequency content at 895 Hz decreases from 8.2% to 1.3%, and that at 1670 Hz decreases from 3.1% to 0.4%. Figure 17(c) demonstrates that the main oscillation frequency contents of 40 Hz, 930 Hz, and 1670 Hz are all suppressed to be less than 1%, which reveals the hybrid mode can effectively inhibit the multi-dimensional oscillation problem in the HIPS.

The combination of the above analyses and experimental validations confirms that the frequency-divided compensation strategy not only considers the actual operation conditions of the power grid, but also adeptly applies various modes to address the complex instability challenges, reducing the corresponding HIPS oscillation frequency to below 2%.

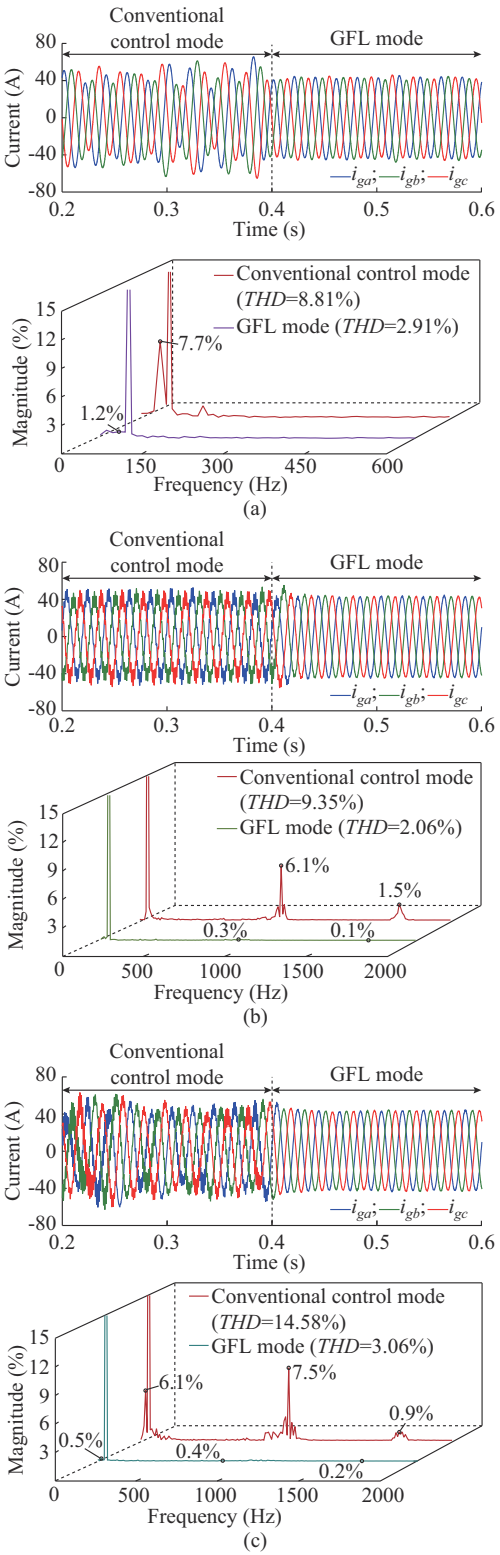

Fig. 16. Simulation verification of frequency-divided compensation strategy for HIPS. (a) GFL mode. (b) GFM mode. (c) Hybrid mode.

VI. Conclusion

This paper establishes the node admittance matrix of HIPS while fully considering PSL, PLL, and delay, thereby laying the foundation for analyzing the multi-dimensional oscillation characteristics of HIPS.

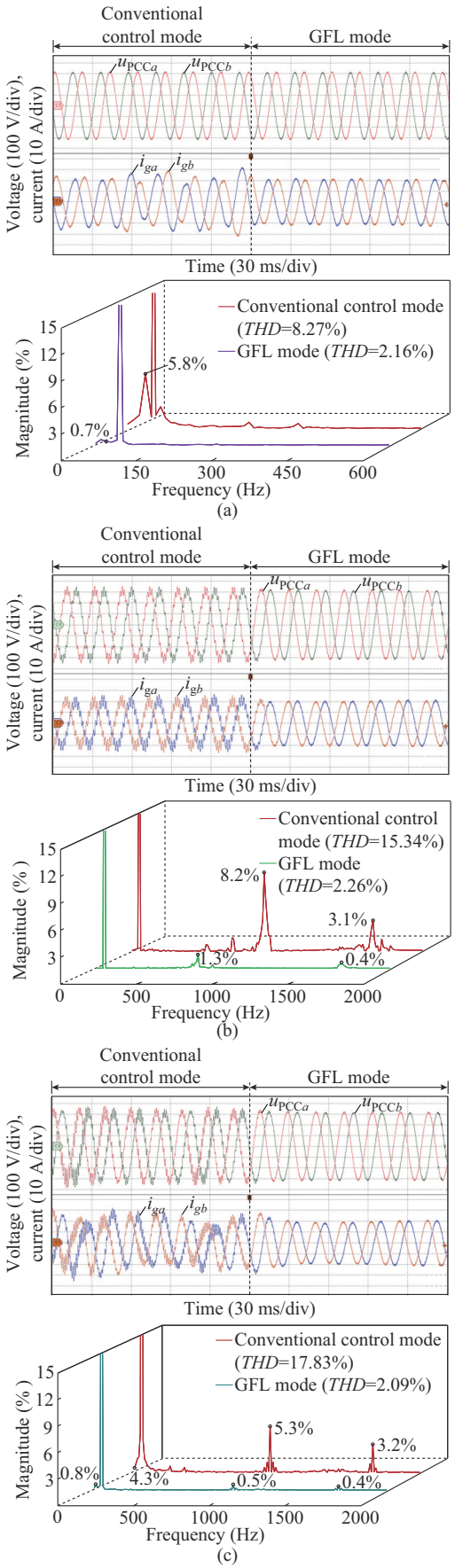

Fig. 17. Experimental verification of frequency-divided compensation strategy for HIPS. (a) GFL mode. (b) GFM mode. (c) Hybrid mode.

Additionally, the modal analysis and parameter sensitivity analysis are employed to identify the dominant factors of HIPS. Furthermore, a frequency-divided compensation strategy is proposed to address the multi-dimensional oscillation problem. The main conclusions are summarized as follows.

1) The constructed interactive admittance matrix model of HIPS fully considers the influences of both inverter and non-inverter factors, i.e., self-admittance and mutual admittance. This model maps the overall system stability to a single inverter, allowing the identification of the resonance-dominant inverter through the modal analysis results.

2) The primary reason for high-frequency oscillation destabilization of HIPS under weak grid conditions is the increased coupling of grid impedance with the current loop of GFL inverter. Conversely, the likelihood of low-frequency oscillation destabilization increases under strong grid conditions, with the voltage loop of GFM inverter being the dominant factor.

3) The frequency-divided compensation strategy classifies the operation modes of HIPS into three categories, i.e., GFM, GFL, and hybrid modes. This strategy dynamically adjusts the operation modes based on real-time harmonic power feedback, suppressing the oscillation frequency content to below 2% and ensuring the stable operation of HIPS.

Although the control strategy proposed in this paper effectively enhances stability, it has certain limitations.

1) GFM inverter is utilized solely as an example of droop control, and further consideration is needed for virtual synchronous generator control, virtual oscillator control, etc.

2) The integration of various types of electronic equipment introduces additional uncertainties to the HIPS, leading to complex fault types, which necessitates further improvements and expansions of the strategy based on actual engineering data.

These limitations provide a direction for future research to explore the potential for further optimizing the technology and advanced control algorithms by integrating the engineering applications with carbon emission reduction benefits.

APPENDIX A

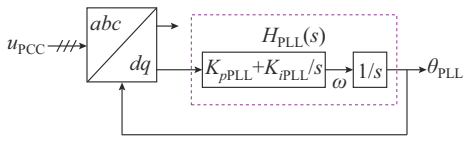

Fig. A1. Structural diagram of PLL based on synchronized coordinate system.

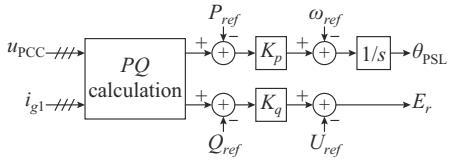

Fig. A2. Structural diagram of PSL based on droop control.

APPENDIX B

$$\begin{cases} T_{\mathrm{p}}(s)=\dfrac{1}{2}\dfrac{H_{\mathrm{PLL}}(s-\mathrm{j}\omega_1)}{1+V_0H_{\mathrm{PLL}}(s-\mathrm{j}\omega_1)}G_d(s) \\ T_{\mathrm{n}}(s)=\dfrac{1}{2}\dfrac{H_{\mathrm{PLL}}(s+\mathrm{j}\omega_1)}{1+V_0H_{\mathrm{PLL}}(s+\mathrm{j}\omega_1)}G_d(s) \end{cases} \tag{B1}$$

$$\begin{cases} Y_1(s)=1+\dfrac{L_{11}C_{\mathrm{f1}}s^2}{C_{\mathrm{f1}}s+1} \\ Y_2(s)=sL_{11}+sL_{21}+\dfrac{L_{11}L_{21}C_{\mathrm{f1}}s^3}{C_{\mathrm{f1}}s+1} \end{cases} \tag{B2}$$

$$C_{\mathrm{p}}(s)=H_{vc}(s-\mathrm{j}\omega_1)H_{vv}(s-\mathrm{j}\omega_1)(\mathrm{j}V_0M(s-\mathrm{j}\omega_1)+N(s-\mathrm{j}\omega_1))\cdot G_d(s)+(\mathrm{j}E_r\mathrm{e}^{\mathrm{j}\theta_{v1}}+\mathrm{j}I_0\mathrm{e}^{\mathrm{j}\varphi_{i0}}H_{vc}(s-\mathrm{j}\omega_1))M(s-\mathrm{j}\omega_1) \tag{B3}$$

$$C_{\mathrm{n}}(s)=H_{vc}(s+\mathrm{j}\omega_1)H_{vv}(s+\mathrm{j}\omega_1)(\mathrm{j}V_0M(s+\mathrm{j}\omega_1)-N(s+\mathrm{j}\omega_1))\cdot G_d(s)+(\mathrm{j}E_r\mathrm{e}^{\mathrm{j}\theta_{v1}}+\mathrm{j}I_0\mathrm{e}^{\mathrm{j}\varphi_{i0}}H_{vc}(s+\mathrm{j}\omega_1))M(s+\mathrm{j}\omega_1) \tag{B4}$$

$$\begin{cases} M(s)=-\dfrac{3k_pG_f(s)}{s} \\ N(s)=-\dfrac{3\mathrm{j}G_f(s)}{k_q} \end{cases} \tag{B5}$$

$$G_f(s)\Big|_{\omega_c=50\pi}=\frac{\omega_c}{s+\omega_c} \tag{B6}$$

$$\begin{cases} Y_3(s)=1+\dfrac{L_{12}C_{\mathrm{f2}}s^2}{C_{\mathrm{f2}}s+1} \\ Y_4(s)=sL_{12}+sL_{22}+\dfrac{L_{12}L_{22}C_{\mathrm{f2}}s^3}{C_{\mathrm{f2}}s+1} \end{cases} \tag{B7}$$

REFERENCES

[1] A. Askarian, J. Park, and S. Salapaka, "Enhanced grid-following (E-GFL) inverter: a unified control framework for stiff and weak grids," *IEEE Transactions on Power Electronics*, vol. 39, no. 5, pp. 5089-5107, May 2024.

[2] L. Fan, Z. Wang, and Z. Miao, "Large angle deviation in grid-following IBRs upon grid voltage dip," *IEEE Transactions on Energy Conversion*, vol. 39, no. 1, pp. 368-378, Mar. 2024.

[3] C. Liyanage, I. Nutkani, L. Meegahapola *et al*., "Stability enhancement of power synchronisation control based grid-forming inverter under varying network characteristics," *IEEE Transactions on Sustainable Energy*, vol. 15, no. 3, pp. 1799-1813, Jul. 2024.

[4] X. Lyu, W. Du, S. M. Mohiuddin *et al*., "Criteria for grid-forming inverters transitioning between current limiting mode and normal operation," *IEEE Transactions on Power Systems*, vol. 39, no. 4, pp. 6107-6110, Jul. 2024.

[5] S. D'Silva, A. Zare, M. B. Shadmand *et al*., "Towards resiliency enhancement of network of grid-forming and grid-following inverters," *IEEE Transactions on Industrial Electronics*, vol. 71, no. 2, pp. 1547-1558, Feb. 2024.

[6] A. Singhal, T. L. Vu, and W. Du, "Consensus control for coordinating grid-forming and grid-following inverters in microgrids," *IEEE Transactions on Smart Grid*, vol. 13, no. 5, pp. 4123-4133, Sept. 2022.

[7] S. P. Me, M. H. Ravanji, M. Z. Mansour *et al*., "Transient stability of paralleled virtual synchronous generator and grid-following inverter," *IEEE Transactions on Smart Grid*, vol. 14, no. 6, pp. 4451-4466, Nov. 2023.

[8] P. Liu, X. Xie, and J. Shair, "Adaptive hybrid grid-forming and grid-following control of IBRs with enhanced small-signal stability under varying SCRs," *IEEE Transactions on Power Electronics*, vol. 39, no. 6, pp. 6603-6607, Jun. 2024.

[9] N. Mohammed, H. Udawatte, W. Zhou *et al*., "Grid-forming inverters: a comparative study of different control strategies in frequency and time domains," *IEEE Open Journal of the Industrial Electronics Society*, vol. 5, pp. 185-214, Mar. 2024.

[10] C. Zhang, X. Li, X. Xing *et al*., "Modeling and mitigation of reso-

nance current for modified LCL-type parallel inverters with inverter-side current control," *IEEE Transactions on Industrial Informatics*, vol. 18, no. 2, pp. 932-942, Feb. 2022.
[11] R. Wang, X. Zhao, Q. Sun *et al*., "Stability analysis of phase locked loops for AC microgrids with hybrid power sources," *IEEE Transactions on Energy Conversion*, vol. 38, no. 2, pp. 1197-1207, Jun. 2023.
[12] A. Sharma and B. K. Panigrahi, "Revisiting small-signal dynamic stability assessment of multi-inverter interfaced grids," *IEEE Systems Journal*, vol. 18, no. 1, pp. 306-314, Mar. 2024.
[13] C. Tu, J. Gao, F. Xiao *et al*., "Stability analysis of the grid-connected inverter considering the asymmetric positive-feedback loops introduced by the PLL in weak grids," *IEEE Transactions on Industrial Electronics*, vol. 69, no. 6, pp. 5793-5802, Jun. 2022.
[14] Y. Li, Y. Gu, and T. C. Green, "Revisiting grid-forming and grid-following inverters: a duality theory," *IEEE Transactions on Power Systems*, vol. 37, no. 6, pp. 4541-4554, Nov. 2022.
[15] P. Ge, C. Tu, F. Xiao *et al*., "Design-oriented analysis and transient stability enhancement control for a virtual synchronous generator," *IEEE Transactions on Industrial Electronics*, vol. 70, no. 3, pp. 2675-2684, Mar. 2023.
[16] J. Yang, C. K. Tse, M. Huang *et al*., "Comparison of homoclinic bifurcations between grid-following and grid-forming converters," *IEEE Transactions on Industrial Electronics*, vol. 71, no. 5, pp. 4731-4741, May 2024.
[17] Z. Tian, X. Li, X. Zha *et al*., "Transient synchronization stability of an islanded AC microgrid considering interactions between grid-forming and grid-following converters," *IEEE Journal of Emerging and Selected Topics in Power Electronics*, vol. 11, no. 4, pp. 4463-4476, Aug. 2023.
[18] L. Hong, W. Shu, J. Wang *et al*., "Harmonic resonance investigation of a multi-inverter grid-connected system using resonance modal analysis," *IEEE Transactions on Power Delivery*, vol. 34, no. 1, pp. 63-72, Feb. 2019.
[19] M. B. Abdelghany, A. Al-Durra, H. Zeineldin *et al*., "Integration of cascaded coordinated rolling horizon control for output power smoothing in islanded wind-solar microgrid with multiple hydrogen storage tanks," *Energy*, vol. 291, p. 130442, Mar. 2024.
[20] M. B. Abdelghany, A. Al-Durra, H. H. Zeineldin *et al*., "A coordinated multitimescale model predictive control for output power smoothing in hybrid microgrid incorporating hydrogen energy storage," *IEEE Transactions on Industrial Informatics*, vol. 20, no. 9, pp. 10987-11001, Sept. 2024.
[21] J. Liu, X. Sun, Z. Chen *et al*., "A hybrid multiresonances suppression method for nonsynchronous LCL-type grid-connected inverter clusters under weak grid," *IEEE Transactions on Power Electronics*, vol. 39, no. 5, pp. 5386-5399, May 2024.
[22] Y. N. Babu and N. P. Padhy, "An approach to improve harmonic attenuation and stability performance in multi-parallel inverter system," *IEEE Transactions on Power Delivery*, vol. 38, no. 5, pp. 3634-3646, Oct. 2023.
[23] W. Wang, X. Shi, G. Wu *et al*., "Interaction between grid-forming converters with AC grids and damping improvement based on loop shaping," *IEEE Transactions on Power Systems*, vol. 39, no. 1, pp. 1905-1917, Jan. 2024.
[24] W. Du, F. K. Tuffner, K. P. Schneider *et al*., "Modeling of grid-forming and grid-following inverters for dynamic simulation of large-scale distribution systems," *IEEE Transactions on Power Delivery*, vol. 36, no. 4, pp. 2035-2045, Aug. 2021.
[25] C. Cheng, S. Xie, Q. Qian *et al*., "Nonlinear modeling and global stability condition of single-phase grid-tied inverter considering SRF-PLL and duty-cycle saturation," *IEEE Transactions on Industrial Electronics*, vol. 69, no. 7, pp. 6973-6983, Jul. 2022.
[26] Y. Tu, J. Liu, Z. Liu *et al*., "Impedance-based analysis of digital control delay in grid-tied voltage source inverters," *IEEE Transactions on Power Electronics*, vol. 35, no. 11, pp. 11666-11681, Nov. 2020.
[27] Y. Guan, Y. Xie, Y. Wang *et al*., "Admittance modeling and stability analysis for inverter-based microgrid with voltage-source-rectifier load," *IEEE Journal of Emerging and Selected Topics in Power Electronics*, vol. 9, no. 2, pp. 1638-1654, Apr. 2021.
[28] S. Chakraborty, S. Patel, G. Saraswat *et al*., "Seamless transition of critical infrastructures using droop-controlled grid-forming inverters," *IEEE Transactions on Industrial Electronics*, vol. 71, no. 2, pp. 1535-1546, Feb. 2024.
[29] T. Wu, C. Chan, Y. Chang *et al*., "Grid-side current improvement with direct digital control and capacitor voltage feedforward to mitigate distorted grid currents for 3Φ3W LCL grid-connected inverter under distorted grid voltages," *IEEE Open Journal of Power Electronics*, vol. 5, pp. 37-49, NOV. 2023.
[30] H. Xu, D. Gan, Q. Zhang *et al*., "A small-signal stability analysis method based on minimum characteristic locus and its application in controller parameter tuning," *IEEE Transactions on Power Systems*, vol. 39, no. 2, pp. 3798-3810, Mar. 2024.
[31] J. Zheng, Y. Zeng, Z. Zhao *et al*., "MPSoC-based dynamic adjustable time-stepping scheme with switch event oversampling technique for real-time HIL simulation of power converters," *IEEE Transactions on Transportation Electrification*, vol. 10, no. 2, pp. 3560-3575, Jun. 2024.
[32] J. Yang, C. K. Tse, and D. Liu, "Sub-synchronous oscillations and transient stability of islanded microgrid," *IEEE Transactions on Power Systems*, vol. 38, no. 4, pp. 3760-3774, Jul. 2023.
[33] S. Liao, Y. Chen, W. Wu *et al*., "Closed-loop interconnected model of multi-inverter-paralleled system and its application to impact assessment of interactions on damping characteristics," *IEEE Transactions on Smart Grid*, vol. 14, no. 1, pp. 41-53, Jan. 2023.

Hongbin Lin received the B.S. and M.S. degrees from the China University of Petroleum (East China), Qingdao, China, in 2021 and 2024, respectively. He is currently working toward the Ph.D. degree in the Key Laboratory of Control of Power Transmission and Conversion, Ministry of Education, Shanghai Jiao Tong University, Shanghai, China. His current research interests include modeling and stability analysis of multi-inverter paralleled system.

Pingjuan Ge received the B.S. degree in electrical engineering from Anhui University, Hefei, China, in 2017, and the Ph.D. degree in electrical engineering from Hunan University, Changsha, China, in 2022. She is currently working as a Lecturer with the New Energy College, China University of Petroleum (East China), Qingdao, China. Her current research interests include modeling and transient stability analysis of power-electronic-based power system.

Hailiang Xu received the B.S. degree in electrical engineering from China University of Petroleum (East China), Qingdao, China, in 2008, and the Ph.D. degree from Zhejiang University, Hangzhou, China, in 2014. He is currently working as a Professor with the New Energy College, China University of Petroleum (East China). His current research interests include renewable energy generation and microgrid.

Yuhan Duan received the B.S. degree from Qingdao University of Science and Technology, Qingdao, China, in 2023. She is currently pursuing a M.S. degree with the College of New Energy, China University of Petroleum (East China), Qingdao, China. Her current research interests include modeling, control, and stability analysis of grid-connected inverter.